An ultrafast and facile nondestructive strategy to convert various inefficient commercial nanocarbons to highly active Fenton-like catalysts

Junhui Wang[a], Qi Fu[a], Jiaxing Yu[a], Huangsheng Yang[a], Zhengping Hao[b], Fang Zhu[a], and Gangfeng Ouyang[a,c,d,1]

[a]Ministry of Education (MOE) Key Laboratory of Bioinorganic and Synthetic Chemistry, School of Chemistry, Sun Yat-Sen University, Guangzhou 510275, Guangdong, China; [b]National Engineering Laboratory for Volatile Organic Compounds (VOCs) Pollution Control Material & Technology, University of Chinese Academy of Sciences, Beijing 101408, China; [c]Chemistry College, Center of Advanced Analysis and Gene Sequencing, Zhengzhou University, Zhengzhou 450001, China; and [d]Provincial Key Laboratory of Emergency Test for Dangerous Chemicals, Guangdong Provincial Engineering Research Center for Ambient Mass Spectrometry, Institute of Analysis, Guangdong Academy of Sciences (China National Analytical Center Guangzhou), Guangzhou 510070, China

Edited by Alexis Bell, Department of Chemical and Biomolecular Engineering, University of California, Berkeley, CA; received August 2, 2021; accepted November 15, 2021

The Fenton-like process catalyzed by metal-free materials presents one of the most promising strategies to deal with the ever-growing environmental pollution. However, to develop improved catalysts with adequate activity, complicated preparation/modification processes and harsh conditions are always needed. Herein, we proposed an ultrafast and facile strategy to convert various inefficient commercial nanocarbons into highly active catalysts by noncovalent functionalization with polyethylenimine (PEI). The modified catalysts could be in situ fabricated by direct addition of PEI aqueous solution into the nanocarbon suspensions within 30 s and without any tedious treatment. The unexpectedly high catalytic activity is even superior to that of the single-atom catalyst and could reach as high as 400 times higher than the pristine carbon material. Theoretical and experimental results reveal that PEI creates net negative charge via intermolecular charge transfer, rendering the catalyst higher persulfate activation efficiency.

Fenton-like catalysis | nanocarbon | noncovalent | n-doping | interface engineering

Due to the rapid pace of urbanization and heavy industrialization, organic pollutants in the aquatic environment have become a serious and ubiquitous problem on a global scale. The Fenton or Fenton-like process, an effective approach to generate active species by activating oxidizing agents for the elimination of a wide range of organic pollutants, has been regarded as a promising strategy to deal with the ever-growing environmental pollution (1, 2). Among the various oxidants, persulfate ($S_2O_8^{2-}$; PS), as an inexpensive, environmentally friendly, and easily handled strong oxidant (E^0 = 2.1 V), has been widely utilized in various fields, including water oxidation (3, 4), chemical analysis (5, 6), microbial/microfluidic fuel cell (7, 8), organic (molecular/polymer) synthesis (9, 10), and environmental remediation (11, 12), ranging from bench-scale experiments to industrial processes. Since originally introduced for in situ soil and groundwater remediation in the late 1990s to overcome the technical limitations of hydrogen peroxide (H_2O_2) (13), the PS-based Fenton-like system has drawn significant attention as an alternative to the H_2O_2-based Fenton process in water/wastewater treatment, owing to the advantages including high oxidation capacity under circumstance conditions (at neutral pH or with background constituents), high-yield radical production, low cost of storage/transportation, and various activation strategies (11, 12). Over the past few years, various transition-metal-based materials have been widely investigated as Fenton-like catalysts for PS activation (14–16). In terms of sustainable development, metal-based catalysts suffer from prohibitive cost, scarcity in nature, and secondary pollution. In this regard, metal-free carbon materials such as carbon nanotubes (CNTs) and graphene are promising candidates, owing to their unique structures and properties (17–19).

In general, the efficiencies of pristine nanocarbons in activation of PS are very low (19, 20). Researchers have successively explored different strategies to boost the PS activation by regulating the local electronic environment of carbocatalysts, such as covalent doping of suitable heteroatoms (e.g., N or S) (17, 21, 22), introduction of intrinsic defects on the edge (23, 24), and construction of specific structure (25). However, the existing strategies usually involve complicated preparation processes (the usage of templates), special equipment (plasma devices), and/or harsh reaction conditions (high-temperature annealing under special atmosphere), which are time-consuming and more laborious, greatly increasing the financial costs for large-scale production and industrialization (22, 25, 26).

In principle, PS activation relies mainly on the cleavage of peroxyl bonds induced by electron transfer from catalysts, and the electron-transfer efficiency could be modulated by tuning the

Significance

The Fenton-like process catalyzed by metal-free materials is one promising strategy for water purification, but to develop catalysts with adequate activity, complicated preparation/modification processes and harsh conditions are always needed, greatly increasing the costs for industrialization. Herein, we developed an ultrafast and facile strategy to convert various inefficient commercial nanocarbons into highly active catalysts by noncovalent functionalization with polyethylenimine (PEI). The n-doping by PEI could create net charge on the carbon plane and greatly enhance the electron mobility, rendering the catalyst much higher persulfate activation efficiency. Such interface engineering represents an innovative, simple, yet effective, strategy for boosting activities of nanocarbons, providing a conceptual advance to design cost-effective and highly efficient catalysts in environmental remediation, chemical synthesis, and fuel-cell applications.

Author contributions: J.W. and G.O. designed research; J.W., Q.F., J.Y., and H.Y. performed research; J.W., Z.H., and F.Z. analyzed data; and J.W., Z.H., F.Z., and G.O. wrote the paper.

The authors declare no competing interest.

This article is a PNAS Direct Submission.

[1]To whom correspondence may be addressed. Email: cesoygf@mail.sysu.edu.cn.

This article contains supporting information online at http://www.pnas.org/lookup/suppl/doi:10.1073/pnas.2114138119/-/DCSupplemental.

Published January 11, 2022.

electron states (i.e., charge/spin density or density of state) of the catalysts (14, 18, 27). Recently, various polyelectrolytes, including polyethylenimine (PEI), have been utilized to tune the surface electronic structures of electrodes in electronic/electrochemical applications (28–31). Inspired by these observations, herein, we explored an ultrafast and facile approach to transform inefficient commercial nanocarbons into highly active, metal-free catalysts for PS activation by noncovalent functionalization with PEI (*SI Appendix*, Scheme S1). Density functional theory (DFT) calculations, X-ray photoelectron spectroscopy (XPS), Raman spectroscopy, and Kelvin probe force microscopy (KPFM) revealed that PEI could tune the local electronic environment of carbon atoms through the intermolecular electron donation from PEI to nanocarbons. As a result, the activities of the modified catalysts could be greatly enhanced and reach as high as 400 times higher than the pristine carbon material. Moreover, PEI-nanocarbon membranes were further in situ fabricated and applied to treat wastewater in a continuous-flow mode, revealing the feasibility of its practical application.

Results and Discussion

Catalytic Performances of the PEI-Nanocarbon/PS Systems. As shown in Fig. 1*A*, the functionalization of multiwalled nanocarbon tubes (MWCNTs; as the representative of the nanocarbons) could be simply achieved via direct addition of PEI aqueous solution into the MWCNT suspensions (including organic pollutants) without any tedious treatment (wash or drying). PEI can be attached to the surfaces of CNTs through noncovalent dispersion interactions based on van der Waals forces, driven by elimination of the hydrophobic interface between the CNT and water (32). As shown in Fig. 1*B*, only C 1s and O 1s are observed for the pristine MWCNT. Upon PEI functionalization, an N 1s peak appears, which comes from the amine groups of the PEI backbone. The thermal gravimetric analysis was also conducted to measure the thermal weight loss of MWCNTs before and after PEI adsorption. Pure PEI could be totally decomposed before 450 °C under N_2 atmosphere (33). As shown in *SI Appendix*, Fig. S1, different from the MWCNT, the PEI-MWCNT exhibits an obvious weight loss from 300 to 450 °C, in accordance with the characteristic decomposition pattern of pure PEI (33), further proving the presence of PEI in the modified composite. Moreover, the water contact angle on the PEI-MWCNT is smaller than that of the pristine MWCNT (*SI Appendix*, Fig. S2), owing to the hydrophilic nature of the coated PEI (32). The nitrogen adsorption/desorption results reveal that the Brunauer–Emmett–Teller (BET) surface area slightly decreases after the functionality of PEI, suggesting that PEI probably occupies some pores of the MWCNT (*SI Appendix*, Fig. S3). Energy-dispersive X-ray (EDX) element mappings for C and N indicate the uniform distribution of N along with the CNT (Fig. 1*C*).

Fenton-like catalytic performance of PEI-MWCNTs was evaluated by activation of PS for bisphenol A (BPA) degradation. After the PEI-MWCNT was in situ fabricated and the adsorption equilibrium of BPA was reached, PS was added into the system to initiate the catalytic reaction (Fig. 1*A*). As shown in Fig. 2*A*, PEI could remarkably enhance the catalytic activity of the MWCNT, and only 3 min are required for the total degradation of BPA. Moreover, as exhibited in Fig. 2*B*, when PS is introduced first, limited BPA degradation could be achieved by the MWCNT/PS system. However, once the PEI solution is subsequently added, BPA is degraded quickly (~40% removal within 30 s) and could also be almost fully removed in 3 min. This indicates that PEI polymer chains could attach on the surface of MWCNTs rapidly (32), leading to the ultrafast in situ preparation of the composite catalyst (within 30 s).

In order to give a clear comparison of the catalytic activities, the BPA degradation kinetics were fitted by the pseudo first-order model (*SI Appendix*, Fig. S4), and the apparent rate constants (k) are listed in *SI Appendix*, Table S1. Notably, the k_{BPA} of the PEI-MWCNT is as high as 144-fold of that of the pristine MWCNT. Moreover, this strategy is versatile and could be extended to various carbon materials, including C_{60}, graphite, graphene oxide, and other CNTs with different surface functional groups, and the BPA degradation rate could be increased as high as 400 times higher than the pristine carbon material (for COOH-MWCNT) (Fig. 2*C*). In addition, it is worthwhile mentioning that the activity of the PEI-MWCNT, with a k-value (14) as high as 12.28 μmol/g/s for BPA degradation, is by far the most impressive catalytic performance among all reported catalysts (see Fig. 2*D* and *SI Appendix*, Table S2 for details).

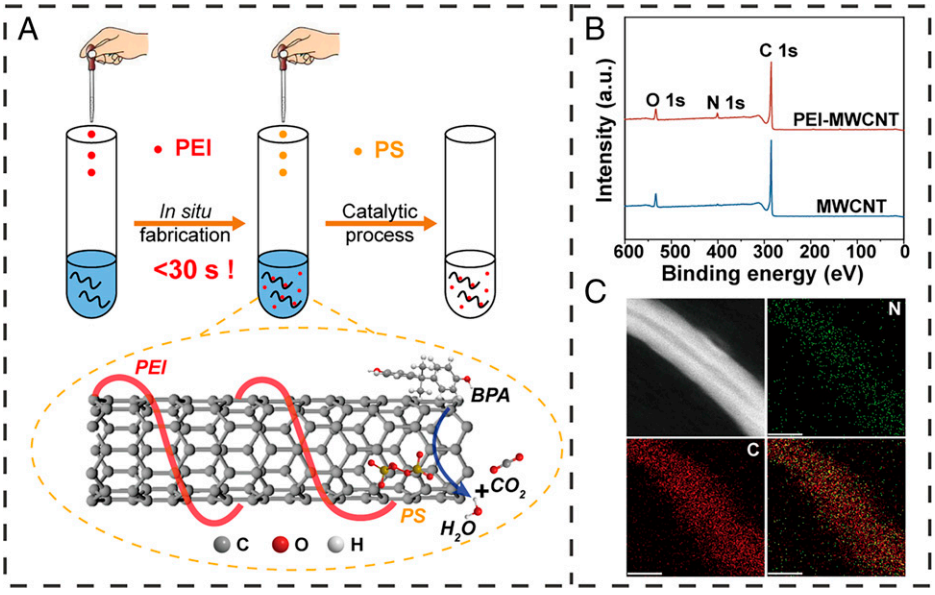

Fig. 1. Fabrication and characterization of the catalysts. (*A*) Schematic illustration of in situ fabrication of the PEI-MWCNT and wastewater treatment process. (*B*) XPS spectra for MWCNT and PEI-MWCNT. A.u., arbitrary units. (*C*) EDX mappings of PEI-MWCNT. (Scale bar: 25 nm.)

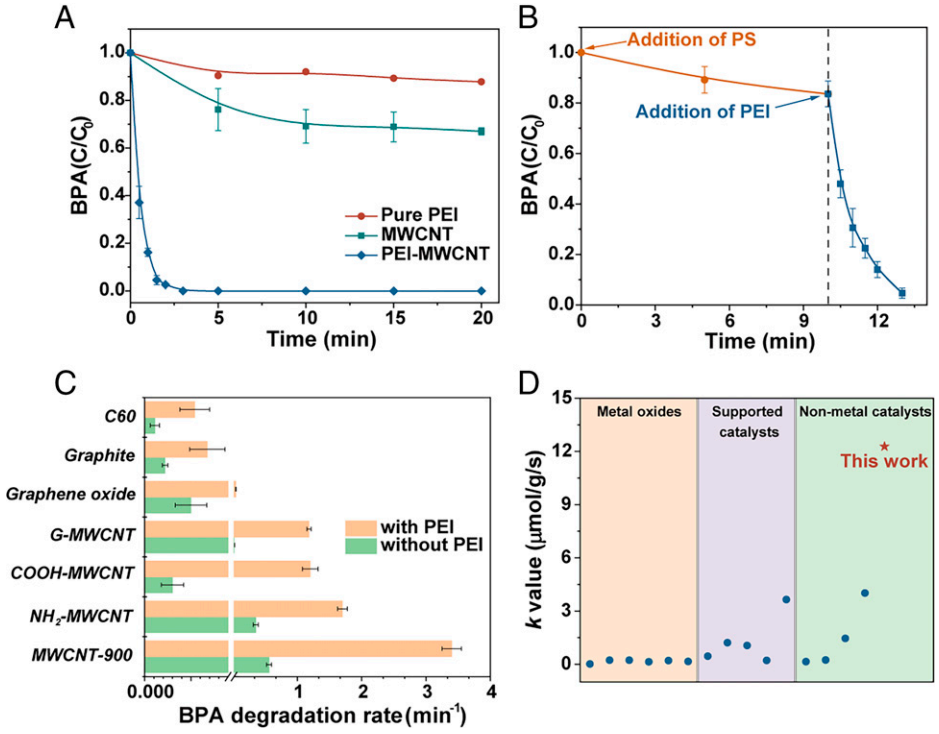

Fig. 2. Catalytic performances of the PEI-nanocarbon/PS systems. (*A*) Catalytic activities of MWCNT, PEI-MWCNT, and pure PEI by PS activation for BPA removal. (*B*) Investigation of the addition sequences of PEI solution on BPA removal. (*C*) Comparison of BPA degradation rates by different carbon materials/PS systems with and without PEI functionalization. (*D*) Comparison of BPA degradation rate constants of the PEI-MWCNT and state-of-the-art catalysts. Reaction conditions: [BPA] = 20 mg/L; [catalyst] = 0.1 g/L; [PS] = 1.5 mM; [PEI solution] = 0.75 mM.

Mechanism Investigation. Electron paramagnetic resonance (EPR) spin-trapping technique and quenching experiments were applied to identify the active species produced during PS activation. As shown in Fig. 3*A*, no signals were observed by using either 5,5-dimethyl-1-pyrroline *N*-oxide (DMPO) or 2,2,6,6-tetramethylpiperidine (TEMP) as the spin adduct. Radical quenching experiments (Fig. 3*B*) also confirmed that radical species merely contributed to the BPA degradation, because the PEI-MWCNT still maintained excellent BPA removal efficiencies at high concentrations (500 mM) of methanol and dimethyl sulfoxide (DMSO) (radical scavenger for ·OH and $SO_4{\cdot}^-$, respectively). These results indicate the presence of active species other than radicals ($SO_4{\cdot}^-$, ·OH) and singlet oxygen ($^1O_2$) during the reaction. However, when triethanolamine (TEA) and ethylenediamine tetraacetic acid disodium (EDTA-2Na), the commonly used hole scavengers, were added into the reaction system, the efficiencies of BPA degradation were significantly reduced. Similar phenomena were also observed in the pristine MWCNT/PS system (Fig. 3*A* and *SI Appendix*, Fig. S5). These results demonstrate that BPA was likely decomposed through an electron-transfer process by reacting with the holes generated on the surface of the catalysts via PS activation.

To further verify the active species in the reaction, the PS activation and reaction processes were investigated by Raman and XPS analyses combined with the PS consumption under different conditions. As exhibited in *SI Appendix*, Fig. S6, after the addition of PS, the characteristic D and G bands of the PEI-MWCNT showed significant upshifts, indicating electron transfer from PEI-MWCNT to PS, consequently generating hole carriers on the surface of the catalyst (28, 34). And if without BPA, the holes could directly oxidize water and subsequently the oxygen intermediates (–OH and –OOH) (35, 36) attached on the carbon plane of the catalyst, as revealed by the increased oxygen content in the XPS spectra (*SI Appendix*, Fig. S7) and the decreased pH value of the reaction solution (*SI Appendix*, Fig. S8). Meanwhile, one PS ion decomposes into two SO_4^{2-} ions, as indicated in *SI Appendix*, Figs. S9 and S10. Moreover, if BPA/EDTA-2Na/TEA (electron donors) added into the PEI-MWCNT/PS system, noticeable decomposition of PS could be observed, and the same amount of EDTA-2Na/TEA could induce a higher PS consumption rate than BPA, due to their higher electron-donating capabilities (*SI Appendix*, Fig. S10). These results clearly reveal that holes induced by PS on the PEI-MWCNT act as the active species for BPA degradation, and the electrons from BPA injected into the holes could then be transferred to PS, leading to its rapid decomposition.

To help in understanding the Fenton-like catalysis in depth, a series of control experiments were performed to explore the main active site(s) for the excellent catalytic performance of the PEI-MWCNT. As shown in *SI Appendix*, Fig. S11, increasing the amount of doped PEI does not induce the enhancement of catalytic performance of MWCNT, indicating that the amine nitrogen ($-NH_2$) species introduced by PEI are not the active sites. Previous studies have suggested that defects (edges and/or vacancies) could act as active sites for PS activation (21, 23). To examine the role of defects in PEI-MWCNT on the catalytic performance, MWCNTs containing different contents of defects were functionalized by PEI and applied to activate PS for BPA degradation (*SI Appendix*, Fig. S12). We can observe that MWCNTs with higher contents of defects could degrade BPA more efficiently, and k_{BPA} presents a positive linear relationship with I_D/I_G ($R^2 = 0.93$) (Fig. 3*C*), which clearly indicate the crucial role of defects for the catalytic activities of PEI-MWCNTs. To further confirm this conjecture, DFT calculations were carried out (*SI Appendix*, Fig. S13), and edge, as one predominant kind of defects in CNT, was selected as a representative of defects in the DFT calculations. As shown in Fig. 3*D*, the stronger adsorption for PS molecule (−3.68 eV) and longer O–O bond length (1.540 Å) on the edge site further indicate that the defects might serve as the active sites for PS activation. Furthermore, the reusability of PEI-MWCNT was also investigated, as

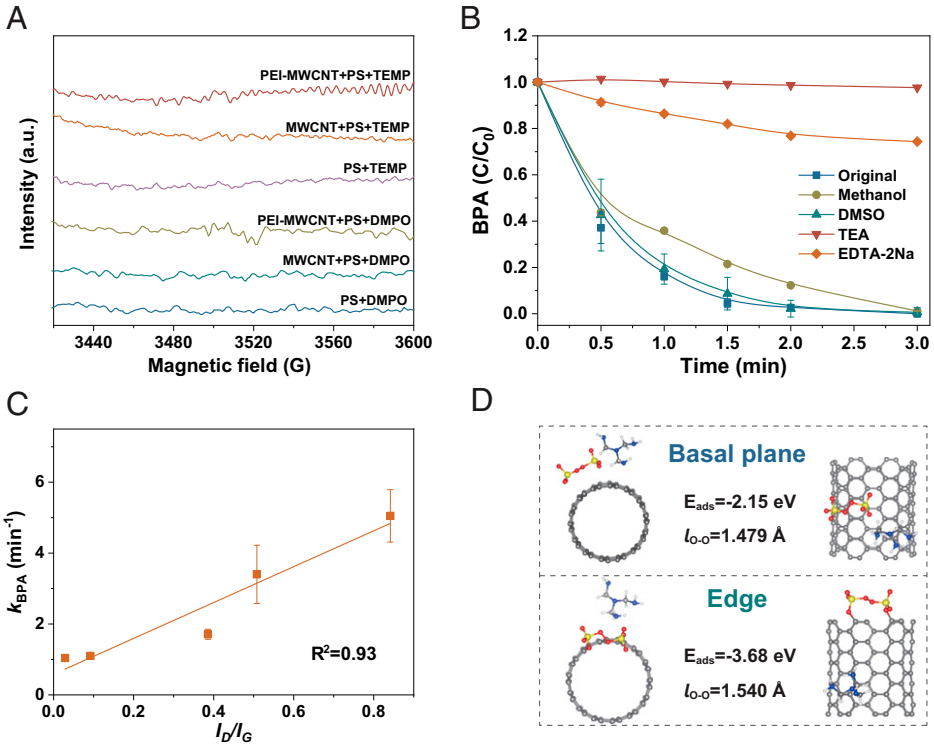

Fig. 3. Investigation for the reaction mechanism and active sites. (*A*) EPR spectra obtained by spin trapping with DMPO and TEMP in the presence of PS and MWCNT/PEI-MWCNT. A.u., arbitrary units. (*B*) Degradation of BPA by the PEI-MWCNT/PS system in the presence of diverse scavengers. (*C*) Dependences of k_{BPA} of different MWCNT catalysts on the values of I_D/I_G. (*D*) Local adsorption configurations and adsorption free energies of PS on the basal plane and edge on PEI-CNT. C, gray; O, red; S, yellow. Reaction conditions: [catalyst] = 0.1 g/L; [PS] = 1.5 mM; [methanol] = 500 mM (if needed); [DMSO] = 500 mM (if needed); [EDTA-2Na] = 50 mM (if needed); [TEA] = 5 mM (if needed).

shown in *SI Appendix*, Fig. S14. The used catalyst exhibited reduced activity (second and third runs), mainly due to the side reaction (water oxidation), which induces oxygen intermediates attached on the catalyst (*SI Appendix*, Fig. S14*B*). After thermal treatment at inert atmosphere, the catalyst could be totally regenerated and showed even higher BPA removal efficiency. As revealed by the Raman spectra (*SI Appendix*, Fig. S15), it can be noticed that after regeneration, the CNT catalyst possesses more defects (higher I_D/I_G), due to the desorption of oxygen-containing functionalities from the CNT lattice at high temperature (*SI Appendix*, Fig. S14*B*) (37). All these results prove the assumption that the intrinsic defects in the PEI-MWCNT catalyst serve as the active sites to activate PS for BPA degradation.

And then, what is the exact role of PEI in the enhanced catalytic performance of the PEI-MWCNT? Considering that PS activation efficiency could be modulated by tuning the electron states (i.e., charge/spin density or density of state) of the catalysts, it can be envisioned that the unique electronic coupling of PEI and MWCNTs plays a crucial role in the significantly enhanced catalytic activity of the PEI-MWCNT. To prove this assumption, XPS analyses and Raman measurements were performed. As shown in Fig. 4*A*, compared to the N 1s peak in pure PEI, that for the PEI-MWCNT exhibited an ∼1.4 eV increase, which implies the presence of charge transfer from PEI to MWCNTs, due to the strong electron-donating capability of abundant amine groups on the PEI backbone (28, 30). Such electronic coupling interaction was verified by Raman spectroscopy (Fig. 4*B*), in which the characteristic G band at 1,583 cm^{-1} associated with the MWCNT showed a downshift by 12 cm^{-1} after PEI functionalization.

To gain an explicit validation of the intermolecular coupling, KPFM measurements were conducted to probe the variation in local work function of the MWCNT surface before and after PEI functionalization (38). The surface topographical and the local contact potential difference (CPD) images of the MWCNT and PEI-MWCNT are shown in Fig. 4 *C*–*F*. The substrate shows a dark contrast; thus, the potential of the sample is higher than that of the fluorine-doped tin oxide (FTO) glass substrate. By analyzing the data in the CPD images, CPD distributions were obtained (Fig. 4 *G* and *H*). Two main peaks reflect the median CPDs of the substrate and sample, and the peak centered at 50 mV belongs to the substrate. For the MWCNT, its median CPD is ∼+175 mV, and, in contrast, that for the PEI-MWCNT is measured to be ∼+150 mV, indicating lower work function of the PEI-MWCNT. DFT calculations were further conducted to confirm the electronic interactions between PEI and the CNT. For the pristine CNT, the work function was determined as 4.76 eV, and that for the PEI-CNT was decreased to 4.72 eV, in accordance with the KPFM data. Moreover, Bader charge analysis was carried out to analyze the exact electron densities of carbon atoms on the CNT before and after PEI adsorption. As displayed in Fig. 4*I*, the carbon atoms nearby the amine group possessed substantially high electron densities (4.040 to 4.150 e) compared with those on a single nanotube (4.000 e). These results clearly indicate that PEI serves as an n-type dopant to donate electrons to the carbon planes of MWCNTs (28). More importantly, as a result, the PEI-CNT demonstrates a prominent increment of electronic states near the Fermi level (*SI Appendix*, Fig. S16), suggesting that the electron mobility in the CNT has been enhanced by PEI functionalization (39, 40). This could also be evidenced by the electrochemical impedance spectroscopy (EIS) Nyquist plots (*SI Appendix*, Fig. S17), in which the arc radii of the PEI-MWCNT electrode were much smaller than those of the MWCNT electrode. It has been measured that after PEI functionalization, the electron mobility in single-

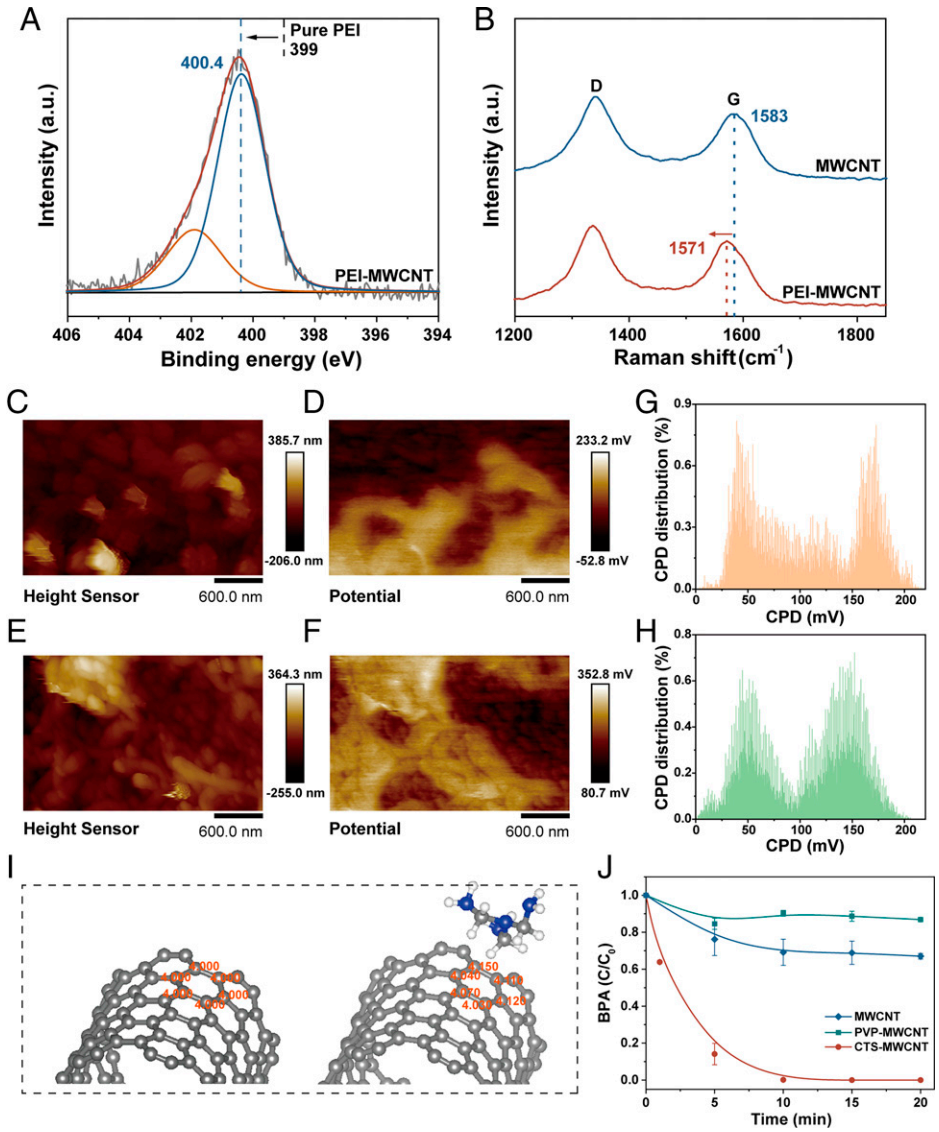

Fig. 4. Investigation of the electronic coupling interaction between PEI and MWCNTs. (*A*) High-resolution N1s XPS spectrum of PEI-MWCNT. (*B*) Raman spectra of MWCNT and PEI-MWCNT. (*C–F*) Surface topographical AFM images (*C* and *E*) and CPD images (*D* and *F*) for MWCNT (*Upper*) and PEI-MWCNT (*Lower*) on FTO glass. (*G* and *H*) CPD distributions of MWCNT (*Upper*) and PEI-MWCNT (*Lower*). (*I*) Calculated charge density distribution of carbon atoms for a single CNT and a CNT attached with one constitutional repeating unit of PEI. (*J*) Catalytic activities of MWCNT, PVP-MWCNT, and CTS-MWCNT by PS activation for BPA removal. A.u., arbitrary units.

walled CNTs (SWCNTs) could be 40-fold higher than the pristine CNTs in the field-effect transistors (41). Therefore, it can be inferred that the increased electron mobility could greatly enhance the reaction rates of PEI-MWCNTs during PS activation and pollutant degradation.

To further examine the effect of the electronic coupling interaction on the catalytic activity of MWCNTs, two kinds of nitrogenous polymers, polyvinyl pyrrolidone (PVP) and chitosan (CTS), were also applied to modify the pristine MWCNT. As evidenced by Raman spectra (*SI Appendix*, Fig. S18), PVP serves as a p-type dopant to attract electrons from the carbon planes. As shown in Fig. 4*J*, PVP doping suppressed the catalytic performance and made the MWCNT nearly deactivated. In contrast, CTS, also with rich amine groups and as n-type dopant (*SI Appendix*, Fig. S18), could also induce a remarkable enhancement of the catalytic activity. These results indicate that the noncovalent n-doping of MWCNT could greatly enhance its catalytic performance for PS activation.

Based on the above investigations, it has been revealed that BPA is degraded by the holes induced by PS on the catalyst via an electron-transferring mechanism. Briefly, PS firstly adsorbs on the defect sites and attracts electrons from the carbon plane, subsequently creating hole carriers on the catalyst. Meanwhile, preadsorbed BPA molecules inject electrons into the holes and are oxidized simultaneously. The electrons from BPA could then be transferred to PS, leading to its rapid decomposition into SO_4^{2-} ions. Furthermore, a plausible mechanism for the greatly enhanced catalytic performance of MWCNTs by PEI functionalization has been proposed (Fig. 5). As demonstrated in our previous work (23), the electrons localized at the highest occupied molecular orbital (HOMO) (−4.76 eV; defined by the work function) of CNT could be injected into the lowest unoccupied molecular orbital (LUMO) of PS (−6.46 eV) due to the energy gap, which induces the generation of holes with oxidation capabilities on CNT. And if more electrons could be extracted by PS, more holes will be generated on CNT, and higher pollutant-removal efficiency will eventually be achieved.

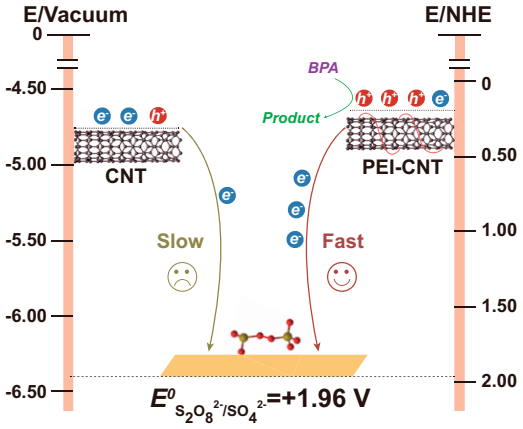

Fig. 5. Plausible mechanism for the boosted catalytic activity of PEI-MWCNT.

It is generally believed that under ambient conditions, CNTs are p-doped (electron-deficient) (42), which is the origin of their poor catalytic performance for PS activation. Benefiting from the electron-donating interaction from PEI to the CNT, the work function of the CNT has been decreased, and net negative charge for carbon atoms could be created in the CNT plane. Therefore, the energy gap between the HOMO of PEI-CNT (−4.72 eV) and the LUMO of PS is larger than that of the pure CNT, and there are more free-flowing p-electrons on the HOMO of the PEI-CNT. Moreover, consequently, the electron mobility in the PEI-CNT has also been greatly enhanced. These three aspects render it easier and faster for PS to attract electrons from the PEI-CNT and to boost the electron transfer from BPA to PS, thus facilitating efficient BPA degradation.

Practical Application Investigation of the PEI-MWCNT/PS System. Due to the ultrafast catalyst-fabrication procedure and rapid degradation for organic pollutants, the practicability of the PEI-MWCNT/PS system was further investigated. As shown in *SI Appendix*, Fig. S19, the PEI-MWCNT/PS exhibits outstanding pH and environmental media adaptabilities, showing similar BPA degradation performance in a broad pH range (2–9) and even actual wastewater. And it also demonstrates excellent degradation activities for different kinds of environmental pollutants, including dyes, antibiotics, and phenolics (*SI Appendix*, Fig. S20).

Furthermore, in order to avoid recycling the dispersed catalysts, membranes were fabricated in situ in a membrane reactor according to our previous report (23). The resultant membranes are 12.56 cm^2 in size and can be easily scaled up (the photographs inserted in *SI Appendix*, Fig. S21*A*). Scanning electron microscopy observations (*SI Appendix*, Fig. S21 *A* and *B*) show an interconnected porous network architecture. As illustrated in *SI Appendix*, Fig. S21*C*, membranes show very high permeances (above 5,700 $L/m^2/h/bar$), and the removal efficiencies of BPA in PEI-MWCNT-20/30 could maintain nearly 100% over 6 h, which is much superior to the reported MoS_2 membrane (90% BPA removal in 6 h and permeance of 154 $L/m^2/h/bar$) (14). We believe that the facile preparation procedure and high catalytic efficiency render PEI-MWCNT an ideal catalyst to remove organic pollutants with low concentration in a continuous-flow mode.

In addition, the PEI leaching was below 0.3 mg/L (only 0.9% of the total PEI on MWCNT) (*SI Appendix*, Fig. S22), indicating that PEI could irreversibly adsorb onto the sidewalls of MWCNTs (41). This could also be evidenced by the constant pH values of the PEI-MWCNT/water suspension, as exhibited in *SI Appendix*, Fig. S8. Moreover, no apparent toxicities were observed for PEI solution and the reaction product of PEI and PS, as revealed by the acute toxicity tests using *Vibrio fischeri* (*SI Appendix*, Fig. S23), suggesting the safety of PEI functionalized catalysts for practical applications.

In summary, rather than conventional covalent doping, we have successfully developed an ultrafast and facile interfacial charge-transfer doping strategy to promote PS activation by nanocarbons via noncovalent functionalization with PEI. Under ambient condition, the modified catalysts could be in situ fabricated by direct addition of PEI aqueous solution into the nanocarbon suspensions without washing and drying. This strategy could greatly enhance the catalytic activities, which could reach as high as 400 times higher than the pristine carbon material. As revealed by experimental and theoretical studies, the electron-donating capability of PEI results in effective "n-doping" of the nanocarbon via directional interfacial charge transfer from PEI to carbons, thereby lowering the work function, creating net negative charge for carbon atoms and enhancing the electron mobility on the PEI-CNT. Furthermore, the PEI-MWCNT could also be fabricated in situ into membranes for water treatment in a continuous-flow mode. This work clearly indicates that other n-type polymers could also be applicable for the development of metal-free efficient Fenton-like catalysts. Therefore, the methodology in this study provides ideas for the design of highly efficient and mass-produced carbon materials for the remediation of practical wastewater and will inspire application of related cocatalysis strategies to other reactions of interest.

Materials and Methods

Chemicals and Materials. The following reagents were used as received: MWCNT (Aladdin; 95%; inner diameter: 3 to 5 nm; outer diameter: 8 to 15 nm; length: 50 μm), NH_2-MWCNT (Aladdin; 95%; inner diameter: 3 to 5 nm; outer diameter: 8 to 15 nm; length: 50 μm), COOH-MWCNT (J&K; 95%; inner diameter: 3 to 5 nm; outer diameter: 8 to 15 nm; length: 50 μm), graphitized (G)-MWCNT (XF NANO; outer diameter: 10 to 20 nm; length: 5 to 30 μm), graphene oxide (J&K), fullerene (C60) (XF NANO), graphite (Aladdin), PEI (linear; molecular weight 70,000; 50 wt.% in H_2O) (Aladdin), PVP (K16-18) (Aladdin), CTS (Aladdin), potassium persulfate (Aladdin), BPA (Sigma-Aldrich), methanol (Sigma-Aldrich), DMSO (Sigma-Aldrich), TEA (Aladdin), EDTA-2Na (Guangzhou Chemical Reagent), potassium iodide (Innochem), methyl red (J&K), methylene blue (Aladdin), phenol (Aladdin), 4-chlorophenol (Aladdin), tetracycline (Aladdin), and sulfamethoxazole (Machlin). Ultrapure deionized water (>18 MΩ·cm), produced with a Millipore system, was used for the preparation of all experimental solutions. All chemicals were of reagent grade and were used without further purification or treatment.

Preparation and Characterization of Polymer-MWCNT. Polymer-functionalized CNTs were in situ prepared as follows. Briefly, under ambient condition, 2 mg of MWCNTs were initially suspended in 20-mL BPA solutions (20 mg/L) by ultrasonication for 30 min. Then, PEI/PVP solutions were added and stirred for 15 min. As for the CTS-MWCNT, in order to make the CTS soluble in water, acetic acid was used to adjust the pH of the solution. Briefly, 100 mg of MWCNTs were initially suspended in 400 mL of ultrapure deionized water in the presence of CTS with monomer concentration of 0.75 mM by ultrasonication for 2 h, and the obtained CNT dispersion was further stirred overnight. After that, the suspension was then centrifugated and washed with water several times, followed by drying in vacuum oven at 60 °C overnight.

In situ fabrication of the PEI-MWCNT membrane. A certain amount of MWCNT (10, 20, or 30 mg) was dispersed in PEI water solution (monomer concentration: 0.75 mM) with a concentration of 0.5 mg of MWCNT/mL and sonicated for 0.5 h. After that, the PEI-MWCNT dispersion was directly filtered on a polyvinylidene fluoride substrate membrane (Millipore; 0.22-μm pore size, 5 cm in diameter) in the homemade membrane reactor with gas pressure of 0.2 bar to in situ fabricate the PEI-MWCNT membrane within 10 min (23). The obtained membranes were denoted as PEI-MWCNT-10, PEI-MWCNT-20, and PEI-MWCNT-30.

XPS analysis was conducted on an ESCALAB 250 spectrometer (Thermo Fisher Scientific Corporation). The binding energies of the recorded XPS spectra were corrected according to the C 1s line at 284.8 eV. After subtracting the Shirley-type background, the core-level spectra were deconvoluted into their

components by using the CasaXPS software. The morphologies of catalysts were observed by using a high-resolution transmission electron microscope (JEM-2010HR, JEOL). The Raman spectra were recorded on a Renishaw InVia Raman spectrometer with a model 100 Ramascope optical fiber instrument using an argon ion laser (excitation at 532 nm). EPR spectra were recorded on a CW/Pulse EPR system (A300, Bruker Co.) under the following conditions: microwave frequency = 9.64 GHz, microwave power = 0.94 mW, modulation frequency = 100 kHz, and modulation amplitude = 2.0 G. The thermogravimetric (TG) curves were obtained by using a TG analyzer (Netzsch-209, Netzsch) from 40 °C to 450 °C under nitrogen atmosphere at the rate of 10 °C/min. BET surface areas were investigated by nitrogen adsorption and desorption at liquid nitrogen temperature (77 K) by using a volumetric adsorption analyzer (ASAP2020, Micromeritics Instrument Corporation). EIS spectra were measured on a three-electrode cell on a CHI 760E workstation (CH Instruments). The composition of the electrodes was the same as that in our previous study (43), and the concentration of Nafion was adjusted to 1 wt.%.

Experimental Procedure and Analytic Methods. The oxidative degradation of organic pollutants by activating PS was performed in magnetically stirred 50-mL reactors at room temperature. A typical experimental suspension contained 100 mg/L MWCNTs and 20 mg/L BPA. After reaching the adsorption equilibrium, the reaction was initiated by adding an aliquot of a prepared solution of PS (150 mM). Samples were withdrawn by using a 1-mL syringe at certain intervals during the reaction, and the solid was removed by filtration (0.22-μm polytetrafluoroethylene filter). The residual concentrations of the target organic compound were analyzed by using a high-performance liquid chromatograph (Shimadzu LC-20AD) equipped with a Poroshell 120 EC-C18 column (4.6 × 100 mm, 2.7 μm; Agilent Technology). The mobile phase comprised water and methanol at a volume ratio of 3:7 with a total flow rate of 0.6 mL/min. The concentration of PS was measured by a spectrophotometric method using potassium iodide suggested by Liang et al. (44). A 0.8-mL sample solution was withdrawn and added into a prepared 3-mL KI water solution (containing 0.015 g $NaHCO_3$ and 0.3 g KI). The resulting solutions were hand shaken and allowed to equilibrate for 15 min for measurement at 352 nm.

PEI leaching was investigated via measuring the total organic carbon (TOC) of the water solutions obtained from the PEI-MWCNT/water suspension after stirring for 60, 180, 360, and 540 min, respectively. TOC was analyzed by using a TOC analyzer (Vario TOC, Elemental). Acute toxicity tests for PEI solution and the reaction product of PEI and PS were performed by using a LUMIStox toxicity analyzer (HACH) based on the reduction of the luminescence emitted by the marine microorganism *V. fischeri*. Toxic substances would affect the enzymatic activity of *V. fischeri*, thereby inhibiting its bioluminescence. The results after 30-min contact periods were reported as luminescence inhibition (percent). To prevent uncorrected toxicity bioassay interpretations, all the samples were diluted to give a final chloride concentration of 3% (45). Duplicate samples were measured for each set of solutions.

DFT Calculation. All the calculations were performed under the scheme of spin-polarized DFT by using the Vienna ab initio simulation package (46). The ion–electron interactions were described by the projector augmented wave method, and the generalized gradient approximation (47) in the Perdew–Burke–Ernzerhof form (48). The cutoff energy for the plane wave was set to 500 eV. The energy criterion was set to 10^{-5} eV in iterative solution of the Kohn–Sham equation. All the structures were relaxed until the residual forces on the atoms declined to less than 5×10^{-3} eV/Å. The weak interaction was described by a DFT-D3 scheme (49). In this work, SWCNTs are taken as an example to consider the catalytic effect for PS adsorption and activation, as shown in *SI Appendix*, Fig. S7. A $C_3H_6N_3H_6$ molecule (repeating a unit of PEI) was used to model the amine-containing thin molecular layer adsorbed on the CNT surface. The simulated CNT was with a size of $a \times b \times c = 10 \times 10 \times 9.838$ Å and built in a cubic simulation cell with lattice content of 30 Å. The vacuum layer was more than 12 Å along three directions to avoid unphysical interaction between the nanotube and the periodic image because of the periodic boundary condition. To investigate the adsorption affinities of PS molecules on different sites of SWCNT and PEI-SWCNT, the adsorption energy was studied by DFT calculations, defined as

$$E_{ads} = E_{total} - E_{substrate} - E_{molecule},$$

where E_{total}, $E_{substrate}$, and $E_{molecule}$ denote the total energy of substrate with adsorbate, substrate, and free molecule, respectively.

Surface Potential Detection by KPFM. Generally, KPFM measures the local CPD between the sample surface and the conducting Pt tip (φ_{sample}–φ_{tip}), which could be used to reflect the change in local work function of the sample by the contrast in the CPD image and profile (38). KPFM was carried out to measure the surface potential of the samples on a Bruker Multimode 8 atomic force microscope (AFM) with the Pt cantilever in a tapping mode. The catalysts were prepared to ink in ethanol (0.2 mL, 1 mg/mL) and deposited onto the cleaned FTO glass electrode (3 cm × 1 cm). The electrode was then dried at 60 °C overnight to totally remove the ethanol and make the sample firmly attached with the FTO glass. The surface potentials of the samples were measured at 200-nm lift height by maintaining a scan speed of 0.996 Hz.

Data Availability. All study data are included in the article and/or *SI Appendix*.

ACKNOWLEDGMENTS. This work was supported by National Natural Science Foundation Projects 21806192, 22036003, 21737006, and 22076222; Science and Technology Program of Guangzhou Project 202102021203; Natural Science Foundation of Guangdong Province Project 2018A030313441; Fundamental Research Funds for the Central Universities Project 19lgpy135; and Guangdong Provincial Key R&D Programme 2020B1111350002.

1. M. A. Shannon *et al.*, Science and technology for water purification in the coming decades. *Nature* **452**, 301–310 (2008).
2. S. S. Gupta *et al.*, Rapid total destruction of chlorophenols by activated hydrogen peroxide. *Science* **296**, 326–328 (2002).
3. F. Evangelisti, R. Moré, F. Hodel, S. Luber, G. R. Patzke, 3d–4f $\{CoII_3Ln(OR)_4\}$ cubanes as bio-inspired water oxidation catalysts. *J. Am. Chem. Soc.* **137**, 11076–11084 (2015).
4. X. B. Han *et al.*, Polyoxometalate-based nickel clusters as visible light-driven water oxidation catalysts. *J. Am. Chem. Soc.* **137**, 5486–5493 (2015).
5. K. Tian, P. K. Dasgupta, A permeable membrane capacitance sensor for ionogenic gases: Application to the measurement of total organic carbon. *Anal. Chim. Acta* **652**, 245–250 (2009).
6. B. Wallace, M. Purcell, J. Furlong, Total organic carbon analysis as a precursor to disinfection byproducts in potable water: Oxidation technique considerations. *J. Environ. Monit.* **4**, 35–42 (2002).
7. Q. Lan *et al.*, Direct formate/persulfate microfluidic fuel cell with a catalyst-free cathode and high power density. *ACS Sustain. Chem. Eng.* **9**, 5623–5630 (2021).
8. N. Li *et al.*, Improved dye removal and simultaneous electricity production in a photocatalytic fuel cell coupling with persulfate activation. *Electrochim. Acta* **270**, 330–338 (2018).
9. H. Shen *et al.*, Trifluoromethylation of alkyl radicals in aqueous solution. *J. Am. Chem. Soc.* **139**, 9843–9846 (2017).
10. S. Mandal, T. Bera, G. Dubey, J. Saha, J. K. Laha, Uses of $K_2S_2O_8$ in metal-catalyzed and metal-free oxidative transformations. *ACS Catal.* **8**, 5085–5144 (2018).
11. B. C. Hodges, E. L. Cates, J. H. Kim, Challenges and prospects of advanced oxidation water treatment processes using catalytic nanomaterials. *Nat. Nanotechnol.* **13**, 642–650 (2018).
12. J. Lee, U. von Gunten, J. H. Kim, Persulfate-based advanced oxidation: Critical assessment of opportunities and roadblocks. *Environ. Sci. Technol.* **54**, 3064–3081 (2020).
13. R. J. Pugh, "In situ remediation of soils containing organic contaminants using the electromigration of peroxysulfate ions." US Patent 5976348 (1999).
14. Y. Chen, G. Zhang, H. Liu, J. Qu, Confining free radicals in close vicinity to contaminants enables ultrafast Fenton-like processes in the interspacing of MoS_2 membranes. *Angew. Chem. Int. Ed. Engl.* **58**, 8134–8138 (2019).
15. X. Li *et al.*, Single cobalt atoms anchored on porous N-doped graphene with dual reaction sites for efficient Fenton-like catalysis. *J. Am. Chem. Soc.* **140**, 12469–12475 (2018).
16. X. Li *et al.*, Topotactic transformation of metal-organic frameworks to graphene-encapsulated transition-metal nitrides as efficient Fenton-like catalysts. *ACS Nano* **10**, 11532–11540 (2016).
17. X. G. Duan, H. Q. Sun, Y. X. Wang, J. Kang, S. B. Wang, N-doping-induced nonradical reaction on single-walled carbon nanotubes for catalytic phenol oxidation. *ACS Catal.* **5**, 553–559 (2015).
18. X. Duan, H. Sun, S. Wang, Metal-free carbocatalysis in advanced oxidation reactions. *Acc. Chem. Res.* **51**, 678–687 (2018).
19. X. G. Duan *et al.*, Insights into heterogeneous catalysis of persulfate activation on dimensional-structured nanocarbons. *ACS Catal.* **5**, 4629–4636 (2015).
20. X. Duan *et al.*, Insights into N-doping in single-walled carbon nanotubes for enhanced activation of superoxides: A mechanistic study. *Chem. Commun. (Camb.)* **51**, 15249–15252 (2015).
21. X. Duan, K. O'Donnell, H. Sun, Y. Wang, S. Wang, Sulfur and nitrogen co-doped graphene for metal-free catalytic oxidation reactions. *Small* **11**, 3036–3044 (2015).
22. X. Wang, Y. Qin, L. Zhu, H. Tang, Nitrogen-doped reduced graphene oxide as a bifunctional material for removing bisphenols: Synergistic effect between adsorption and catalysis. *Environ. Sci. Technol.* **49**, 6855–6864 (2015).
23. J. Wang *et al.*, Unprecedented nonphotomediated hole (h^+) oxidation system constructed from defective carbon nanotubes and superoxides. *ACS Cent. Sci.* **7**, 355–364 (2021).
24. W. Ren *et al.*, Insights into the electron-transfer regime of peroxydisulfate activation on carbon nanotubes: The role of oxygen functional groups. *Environ. Sci. Technol.* **54**, 1267–1275 (2020).

25. C. Chu *et al.*, Cooperative pollutant adsorption and persulfate-driven oxidation on hierarchically ordered porous carbon. *Environ. Sci. Technol.* **53**, 10352–10360 (2019).
26. Y. Gao, Z. Chen, Y. Zhu, T. Li, C. Hu, New insights into the generation of singlet oxygen in the metal-free peroxymonosulfate activation process: Important role of electron-deficient carbon atoms. *Environ. Sci. Technol.* **54**, 1232–1241 (2020).
27. X. Chen, W. D. Oh, T. T. Lim, Graphene- and CNTs-based carbocatalysts in persulfates activation: Material design and catalytic mechanisms. *Chem. Eng. J.* **354**, 941–976 (2018).
28. C. S. Mo *et al.*, Boosting water oxidation on metal-free carbon nanotubes via directional interfacial charge-transfer induced by an adsorbed polyelectrolyte. *Energy Environ. Sci.* **11**, 3334–3341 (2018).
29. S. Wang, D. Yu, L. Dai, Polyelectrolyte functionalized carbon nanotubes as efficient metal-free electrocatalysts for oxygen reduction. *J. Am. Chem. Soc.* **133**, 5182–5185 (2011).
30. Y. Zhou *et al.*, A universal method to produce low-work function electrodes for organic electronics. *Science* **336**, 327–332 (2012).
31. S. Wang, D. Yu, L. Dai, D. W. Chang, J.-B. Baek, Polyelectrolyte-functionalized graphene as metal-free electrocatalysts for oxygen reduction. *ACS Nano* **5**, 6202–6209 (2011).
32. S. Zhang *et al.*, Polyethylenimine-enhanced electrocatalytic reduction of CO_2 to formate at nitrogen-doped carbon nanomaterials. *J. Am. Chem. Soc.* **136**, 7845–7848 (2014).
33. X. Zeng *et al.*, Simultaneously tuning charge separation and oxygen reduction pathway on graphitic carbon nitride by polyethylenimine for boosted photocatalytic hydrogen peroxide production. *ACS Catal.* **10**, 3697–3706 (2020).
34. A. M. Rao, P. C. Eklund, S. Bandow, A. Thess, R. E. Smalley, Evidence for charge transfer in doped carbon nanotube bundles from Raman scattering. *Nature* **388**, 257–259 (1997).
35. H. B. Tao *et al.*, A general method to probe oxygen evolution intermediates at operating conditions. *Joule* **3**, 1498–1509 (2019).
36. Y. Xu, M. Kraft, R. Xu, Metal-free carbonaceous electrocatalysts and photocatalysts for water splitting. *Chem. Soc. Rev.* **45**, 3039–3052 (2016).
37. P. G. Collins, *Defects and Disorder in Carbon Nanotubes* (Oxford University Press, Oxford, UK, 2010).
38. J. Y. Cheon *et al.*, Intrinsic relationship between enhanced oxygen reduction reaction activity and nanoscale work function of doped carbons. *J. Am. Chem. Soc.* **136**, 8875–8878 (2014).
39. Z. Hong *et al.*, Rational design and general synthesis of S-doped hard carbon with tunable doping sites toward excellent Na-ion storage performance. *Adv. Mater.* **30**, e1802035 (2018).
40. S. Huang *et al.*, N-doping and defective nanographitic domain coupled hard carbon nanoshells for high performance lithium/sodium storage. *Adv. Funct. Mater.* **28**, 1706294 (2018).
41. M. Shim, A. Javey, N. W. Kam, H. Dai, Polymer functionalization for air-stable n-type carbon nanotube field-effect transistors. *J. Am. Chem. Soc.* **123**, 11512–11513 (2001).
42. V. Schroeder, S. Savagatrup, M. He, S. Lin, T. M. Swager, Carbon nanotube chemical sensors. *Chem. Rev.* **119**, 599–663 (2019).
43. J. H. Wang *et al.*, Highly efficient removal of organic pollutants by ultrahigh-surface-area-ethynylbenzene-based conjugated microporous polymers via adsorption-photocatalysis synergy. *Catal. Sci. Technol.* **8**, 5024–5033 (2018).
44. C. Liang, C.-F. Huang, N. Mohanty, R. M. Kurakalva, A rapid spectrophotometric determination of persulfate anion in ISCO. *Chemosphere* **73**, 1540–1543 (2008).
45. Z. Wu *et al.*, Roles of reactive chlorine species in trimethoprim degradation in the UV/chlorine process: Kinetics and transformation pathways. *Water Res.* **104**, 272–282 (2016).
46. G. Kresse, D. Joubert, From ultrasoft pseudopotentials to the projector augmented-wave method. *Phys. Rev. B Condens. Matter Mater. Phys.* **59**, 1758–1775 (1999).
47. J. P. Perdew, K. Burke, M. Ernzerhof, Generalized gradient approximation made simple. *Phys. Rev. Lett.* **77**, 3865–3868 (1996).
48. J. P. Perdew, M. Ernzerhof, K. Burke, Rationale for mixing exact exchange with density functional approximations. *J. Chem. Phys.* **105**, 9982–9985 (1996).
49. S. Grimme, Semiempirical GGA-type density functional constructed with a long-range dispersion correction. *J. Comput. Chem.* **27**, 1787–1799 (2006).